Mechatronics 56 (2018) 157–165

Contents lists available at ScienceDirect

Mechatronics

journal homepage: www.elsevier.com/locate/mechatronics

Application of robust monotonically convergent spatial iterative learning control to microscale additive manufacturing☆

Zhi Wang[a], Christopher P. Pannier[b], Kira Barton[b], David J. Hoelzle[c,*]

[a] Dept. of Aerospace and Mechanical Engineering, 225 Multidisciplinary Research Building, University of Notre Dame, Notre Dame, IN 46556, USA
[b] Dept. of Mechanical Engineering, University of Michigan, 2350 Hayward Street, Ann Arbor, MI 48109, USA
[c] Dept. of Mechanical and Aerospace Engineering, The Ohio State University, 201 West 19th Avenue Columbus, OH 43210, USA

ARTICLE INFO

Keywords:
Iterative learning control
Additive manufacturing
Electrohydrodynamic jet printing
Run-to-run control
Manufacturing processes

ABSTRACT

Microscale additive manufacturing μ-AM processes are a class of manufacturing processes used to fabricate micron-sized structures in a sequence of direct additions of materials as instructed by a digital file, as opposed to the lithographic patterning and subtractive etching used in traditional microscale manufacturing. Despite being sophisticated, numerically controlled tools, material addition is an open-loop process which requires continual user intervention to heuristically tune process parameters. This paper details the first experimental demonstration of a run-to-run feedback algorithm termed Spatial Iterative Learning Control (SILC), a framework previously introduced by the authors to enable robust, auto-regulation of sensitive μ-AM processes [1, 2]. We demonstrate that SILC enables us to autonomously fabricate complex topography structures with as small as 5 μm x- and y-axis resolution and ∼ 113 nm feature height accuracy, without any heuristic tuning by a user. Lastly, it was observed that an SILC design was robust to system faults, as demonstrated by the ability to recover from both an actuator and sensor fault in two iterations.

1. Introduction

Microscale manufacturing is the production of goods with designed features on the micrometer length scale [3–5]. Lithographic micromachining has been the 'gold standard' for microscale patterning since the 1960s; lithographic micromachining consists of a sequence of material film depositions, photolithographic patternings, and then chemical etchings to subtractively remove unwanted film materials [6]. Lithographic micromachining is limited by: a reliance on fixed photomasks; a reliance on a photoresist, which relegates lithography to be an indirect method for most applications where materials of interests are chemically etched using the photoresist as an etch mask; serial processing where typically only one material is patterned (etched) in one step; and the toxicity of photoresist and etch chemistries that create an environmental and safety hazard and denature biological materials that could be used for biosensors [7] and self-assembly [8]. A generation of new microscale manufacturing modalities has focused on addressing these key limitations. In general, these new modalities are:

- **Direct:** building constructs with the actual build material and using little or no sacrificial masking or supporting materials
- **Parallel:** fabricating with multiple disparate material chemistries on a single tool
- **Facile:** expanding the design space to include non-planar, or graded topographies
- **Environmentally friendly:** using small-to-zero quantities of toxic chemicals and with the potential for direct fabrication from biological materials.

Microscale manufacturing tools with these capabilities are in a broad class called direct-write microscale additive manufacturing (μ-AM) tools. In general, material is delivered in the liquid-phase. The liquid-phase characteristic enables the benefits of being direct, parallel, facile, and environmentally friendly; however, patterning is challenged because nanoscale physical phenomena such as surface energy and electrostatics-dominated kinetics [9] and sensitivity to the local environment influences material placement [10], hence patterning. Additionally, at current laboratory scales, inks are made in small designer batches, leading to inconsistency in process behavior.

Currently, μ-AM tools are controlled in open-loop, where trained users build process maps via heuristic tuning and design-of-experiments methods. As the fabricated features can only be resolved by optical [11,12] or scanning electron microscopy or atomic force microscopy (AFM) [11] or interferometric profilometry [13], the user may only quantify deviations from desired behavior post-process and then forensically determine corrective actions. This time lag in corrective action

☆ This paper was recommended for publication by Associate Editor Chennai Guest Editor.

* Corresponding author.
E-mail addresses: zwang10@nd.edu (Z. Wang), pannier@umich.edu (C.P. Pannier), bartonkl@umich.edu (K. Barton), hoelzle.1@osu.edu (D.J. Hoelzle).

https://doi.org/10.1016/j.mechatronics.2018.09.003
Received 28 October 2017; Received in revised form 10 July 2018; Accepted 10 September 2018
Available online 3 October 2018

increases costs and decreases part quality. To truly elevate μ-AM to be production instruments, we need automatic control solutions to regulate the μ-AM process to achieve a desired part topography. Unfortunately, two challenges preclude real-time sensor integration. (1) The μ-AM dynamic timescale is on the order of microseconds and is thus much faster than aforementioned slow metrology systems [5,14]. (2) Fast, laser-based metrology systems are difficult to place *in situ*, at the location of liquid-phase material delivery.

The unique challenges of μ-AM motivated the design of spatial iterative learning control (SILC), a control algorithm designed to autoregulate μ-AM systems on a run-to-run, or part-to-part, basis [2]. Recently, this basic framework has been extended to consider process uncertainty, defining bounds on algorithm convergence for uncertain systems [1]. This manuscript describes the first complete experimental validation of SILC applied to spatial interval systems; previous experimental implementations looked at much simpler reference functions and tasks [15]. The purpose of this manuscript is to provide a detailed description of an experimental setup and validation to serve as a model of an SILC application. As such, we provide only the salient details of SILC, and we invite those interested in a full description of the SILC framework and theory to consult [1,2]. The salient details of SILC, importantly the definition of systems with spatial dynamics in the lifted-domain, are provided in Section 2. The details of the SILC case application study is provided in Sections 3 and 4. Here, we apply SILC to the μ-AM process electrohydrodynamic jet (e-jet) printing with an integrated AFM sensor to measure the topography of fabricated structures. The control objective is to autonomously learn the appropriate input signal to the e-jet system such that a part with the desired topography map is printed. Experimental results (Section 5) demonstrate that SILC improves process performance and is robust to actuator and sensor errors, as well as stochastic plants. The paper concludes with a discussion of the results and future directions (Section 6).

2. Spatial iterative learning control framework

This section serves to briefly introduce the lifted-domain systems representations of spatial systems, the SILC update law, and basic stability, convergence, and robust monotonic convergence (RMC) criteria. To simplify the treatment, this paper does not address the spatial frequency-domain framework; those interested in the frequency-domain or a more complete description of SILC theory should reference [1] and [2]. In its current form, SILC is applicable to systems with purely spatial dynamics in 2-D: systems defined by a spatial operator $g = Hf$, where a spatial input, $f(x, y)$, is mapped to an output, $g(x, y)$ by spatial operator H. We assume the operator to be spatially-invariant, linear, and stochastic; spatially-varying dynamics are bounded by uncertainty intervals.

We use $\mathbb{Z}$ to represent the set of integers, and $\mathbb{N}$ is its nonnegative subset. For an odd positive integer n,

$$\mathbb{Z}_n \triangleq \{(1-n)/2, (3-n)/2, \dots, (n-1)/2\}.$$

A generic function sampled at discrete values, $p(x, y)$ where $(x, y) \in \mathbb{Z}_M \times \mathbb{Z}_N$, will be interchangeably referred to as a function or its matrix form

$$p(x,y) = \begin{bmatrix} p\left(\frac{1-M}{2}, \frac{1-N}{2}\right) & p\left(\frac{1-M}{2}, \frac{3-N}{2}\right) & \cdots & p\left(\frac{1-M}{2}, \frac{N-1}{2}\right) \\ p\left(\frac{3-M}{2}, \frac{1-N}{2}\right) & p\left(\frac{3-M}{2}, \frac{3-N}{2}\right) & \cdots & p\left(\frac{3-M}{2}, \frac{N-1}{2}\right) \\ \vdots & \vdots & \ddots & \vdots \\ p\left(\frac{M-1}{2}, \frac{1-N}{2}\right) & p\left(\frac{M-1}{2}, \frac{3-N}{2}\right) & \cdots & p\left(\frac{M-1}{2}, \frac{N-1}{2}\right) \end{bmatrix}.$$

We define the operator $\mathcal{V}(p) \triangleq \text{vec}(p^T)$, where vec(.) is the conventional (columnwise) vectorization operator.

2.1. Spatial plants with known dynamics

Consider a plant defined by a known spatial operator H_o. By leveraging the spatial invariance assumption, the operator, H_o, can be reframed as 2-D convolution of a known, nominal spatial impulse response function $h_o(x, y)$ and the input function $f_j(x, y)$, where $j \in \mathbb{N}$ is the iteration index,

$$\begin{aligned} g_j(x,y) &= \left(f_j * h_o\right)(x,y) \\ &= \sum_{\substack{m\in\mathbb{Z}_M \\ n\in\mathbb{Z}_N}} h_o(x-m, y-n) f_j(m,n) \end{aligned} \tag{1}$$

and $g_j(x, y)$ is the output function.

Remark 1. Eq. (1) formalizes the addition of material at steady-state as the superposition of individual material addition events, such as the ejection of a droplet of material, where each material addition event is modeled as the material addition topography, convolution kernel h_o, scaled by the input magnitude at that spatial location, $f_j(m, n)$.

2.2. Lifted-Domain representation

The 2-D convolution systems representation in (1) can be written in the lifted-domain[1],

$$\mathbf{g}_j = \mathbf{H_o} \mathbf{f}_j.$$

$\mathbf{f}_j = \mathcal{V}(f_j) \in \mathbb{R}^{MN\times 1}$ and $\mathbf{g}_j = \mathcal{V}(g_j) \in \mathbb{R}^{MN\times 1}$. The spatial dynamics matrix $\mathbf{H_o} \in \mathbb{R}^{MN\times MN}$ is a Block Circulant matrix with Circulant Blocks (BCCB) composed of the entries of the impulse response h_o. BCCB matrices have inherent repetition of terms which can be leveraged to improve SILC computational efficiency [2]; readers interested in the details of BCCB matrices and their computationally efficient uses should reference [1,16,17].

2.3. Interval uncertain spatial plants

As motivated by previous work on interval uncertain temporal plants [18,19], an interval uncertain spatial plant is a plant whose spatial impulse response is bounded within some interval. The true spatial impulse response h is unknown, but bounded by constant functions: $\underline{h}(x, y) \le h(x, y) \le \overline{h}(x, y)\ \forall (x, y)$. In the lifted-domain, the true plant BCCB matrix $\mathbf{H}$ is unknown, but bounded by constant functions: $\underline{\mathbf{H}} \preceq \mathbf{H} \preceq \overline{\mathbf{H}}$. $\underline{\mathbf{H}}$ and $\overline{\mathbf{H}}$ denote the plant BCCB matrices for certain plants whose spatial impulse responses are $\overline{h}$ and $\underline{h}$, respectively, and $\preceq$ denotes the element-wise $\le$: $\mathbf{A}\preceq\mathbf{B}$ denotes $a_{ij} \le b_{ij}\ \forall i, j$. The convention in interval uncertain systems is to define the nominal system as the center of the uncertainty interval $\mathbf{H_o} = \frac{\underline{\mathbf{H}}+\overline{\mathbf{H}}}{2}$.

Remark 2. Analogous to Remark 1, the interval uncertain plant representation formalizes the observation that material addition is a stochastic process. Convolution kernels $\underline{h}$ and $\overline{h}$ bound the material addition topography in the vicinity of a material addition event.

2.4. SILC Design

The SILC update law has the same form as the temporal ILC law; however, SILC uses 2-D convolution instead of 1-D,

$$f_{j+1}(x,y) = (l_f * f_j)(x,y) + (l_e * e_j)(x,y), \tag{2}$$

where $l_f(x, y)$ and $l_e(x, y)$ are spatial impulse responses of the input updating filter and error updating filter, respectively, and $e_j(x, y) = g_d(x, y) - g_j(x, y)$ is the error function, where $g_d(x, y)$ is the desired output function (or reference function). We use w as the iteration shift operator: $wf_j = f_{j+1}$. A schematic of SILC is given in Fig. 1. The SILC updating law in (2) can be written in the lifted-form as well,

$$\mathbf{f}_{j+1} = \mathbf{L_f} \mathbf{f}_j + \mathbf{L_e} \mathbf{e}_j.$$

Most standard ILC design methods, such as proportional type, model-inverse design, and norm-optimal (NO) designs, can be employed by

[1] Bold-faced characters denote signals and systems in the lifted-domain.

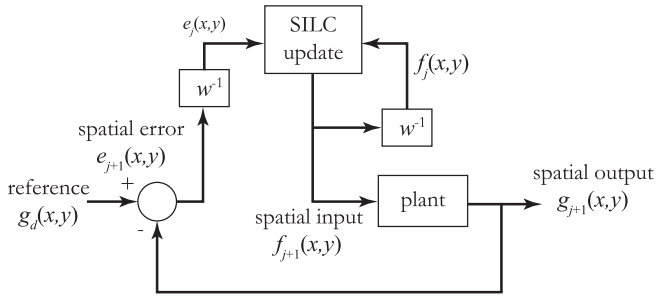

Fig. 1. Block diagram of SILC. w is the iteration shift operator.

SILC. Here, we demonstrate NO-SILC, which aims to minimize the objective function

$$\mathcal{J} = \mathbf{e}_{j+1}^T \mathbf{Q} \mathbf{e}_{j+1} + \mathbf{f}_{j+1}^T \mathbf{S} \mathbf{f}_{j+1} + (\mathbf{f}_{j+1} - \mathbf{f}_j)^T \mathbf{R} (\mathbf{f}_{j+1} - \mathbf{f}_j)$$

where $\mathbf{Q} \in \mathbb{R}^{MN \times MN}$, $\mathbf{S} \in \mathbb{R}^{MN \times MN}$, and $\mathbf{R} \in \mathbb{R}^{MN \times MN}$ are positive definite weighting matrices that penalize a norm on the error, a norm on the input, and a norm on the change in input with respect to iteration, respectively. Generally, **Q, S, R** need not be BCCB matrices; however, the trivial BCCB matrices, $\mathbf{Q} = q\mathbf{I}, \mathbf{S} = s\mathbf{I}, \mathbf{R} = r\mathbf{I}$, with $\{q, s, r\}$ positive real numbers, are a common selection and are used here; $\mathbf{I}$ is the appropriately sized identity matrix. As given in [2,20], the NO-SILC learning filters for $\mathbf{Q} = q\mathbf{I}, \mathbf{S} = s\mathbf{I}, \mathbf{R} = r\mathbf{I}$ are given by

$$\begin{aligned} \mathbf{L_f} &= \left(q\mathbf{H_o}^T\mathbf{H_o} + s\mathbf{I} + r\mathbf{I}\right)^{-1}\left(r\mathbf{I} + q\mathbf{H_o}^T\mathbf{H_o}\right) \\ \mathbf{L_e} &= \left(q\mathbf{H_o}^T\mathbf{H_o} + s\mathbf{I} + r\mathbf{I}\right)^{-1} q\mathbf{H_o}^T, \end{aligned} \tag{3}$$

where $\mathbf{H_o}$ is the lifted-form of the identified center system.

2.5. SILC Stability and monotonic convergence criteria

2.5.1. Spatial plants with known dynamics

The iteration-domain stability and monotonic convergence criterion for known plants follows directly from well-known temporal ILC theory; we provide detailed stability theorems and proofs for SILC in [2]. Briefly, an SILC update law with $\mathbf{L_f}$ and $\mathbf{L_e}$ designed to be BCCB matrices and applied to a known plant, $\mathbf{H_o}$, is stable and monotonically convergent if

$$\rho\left(\mathbf{L_f} - \mathbf{L_e}\mathbf{H_o}\right) = \bar{\sigma}\left(\mathbf{L_f} - \mathbf{L_e}\mathbf{H_o}\right) < 1,$$

where ρ and $\bar{\sigma}$ are the spectral radius and maximum singular value operators, respectively.

2.5.2. Interval uncertain spatial plants

The iteration-domain stability and RMC criterion for interval uncertainty plants is described in detail in [1]. Briefly, an SILC update law with $\mathbf{L_f}$ and $\mathbf{L_e}$ designed to be BCCB matrices and applied to an interval uncertain plant, $\underline{\mathbf{H}} \preceq \mathbf{H} \preceq \overline{\mathbf{H}}$, is stable and RMC if

$$||\left(\overline{\mathbf{H}} - \underline{\mathbf{H}}\right)/2||_2 \leq \frac{1 - ||\mathbf{L_f} - \mathbf{L_e}\mathbf{H_o}||_2}{||\mathbf{L_e}||_2}, \tag{4}$$

where $||\cdot||_2$ denotes the induced 2-norm.

Remark 3. For NO-SILC designs such that $\mathbf{Q} = \mathbf{I}, \mathbf{S} = s\mathbf{I}, \mathbf{R} = r\mathbf{I}$, parameters s and r determine whether or not the RMC criterion is satisfied and there is always a choice (s^*, r^*) such that the RMC criterion is satisfied. Hence, the $s - r$ design space can be partitioned into regions in which the RMC criteria is satisfied and regions in which it is not. Consider the partition function, possibly a multivalued function, $r = c(s)$ such that

$$||\left(\overline{\mathbf{H}} - \underline{\mathbf{H}}\right)/2||_2 = \frac{1 - ||\mathbf{L_f}(r,s) - \mathbf{L_e}(r,s)\mathbf{H_o}||_2}{||\mathbf{L_e}(r,s)||_2}.$$

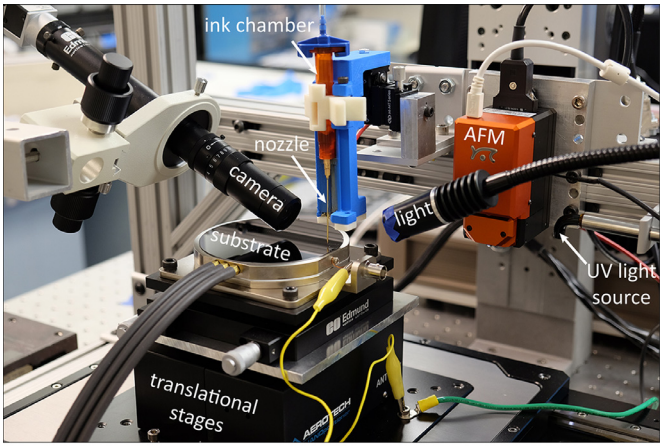

Fig. 2. Integrated e-jet/AFM system setup photo. The system is housed in the Barton Research Group at the University of Michigan.

For a NO-SILC design of (s^*, r^*) not on this partition function, we define the RMC radius

$$R_{\mathrm{RMC}}(r^*, s^*) = \min_s \sqrt{\left(r^*_{\mathrm{dB}} - c(s)_{\mathrm{dB}}\right)^2 + \left(s^*_{\mathrm{dB}} - s_{\mathrm{dB}}\right)^2}$$

where subscript dB denotes the standard decibel transform. Intuitively, $R_{\mathrm{RMC}}(s^*, r^*)$ provides a scale factor for which a design exceeds or satisfies the RMC criterion; we choose the convention employed by the standard gain margin and phase margin that a negative R_{RMC} denotes RMC criterion not satisfied and a positive R_{RMC} denotes RMC criterion satisfied. Note that the partition function $c(s)$ will not have a closed-form expression, in general. In Tb. 2 we compute R_{RMC} by numerical sampling with a fine grid.

3. System description

The purpose of this demonstration is to provide an application model such that users can map SILC and the RMC criterion evaluation to other application classes. To do so, we describe the evaluation of the RMC criterion and a simulated and experimental performance on a system with spatial dynamics, spatial actuation, and a spatial sensor.

3.1. Overview

SILC is applied to an e-jet system with integrated topographical sensing by AFM (Fig. 2); e-jet is a liquid-phase μ-AM tool for fabricating structures on a substrate with feature sizes as small as $\sim$50 nm. The input f to the e-jet tool is a material ejection stimulus applied at each coordinate on a discretized 2-D domain (Fig. 3); the ejection mechanism specifics are provided in Section 3.2. The output of the e-jet tool is the average material height over a discretized coordinate; material height is measured by AFM and then the output function is the image processed signal from the raw AFM scan. The combined e-jet/AFM system is an apt test of SILC: 1) e-jet material accumulation has spatial dynamics at steady-state – material ejected at a spatial coordinate (m, n) increases the material height at coordinate (m, n) and adjacent coordinates (e.g. $(m+1, n)$); and 2) an AFM is an offline measurement tool that provides topography measurement at each location in the 2-D domain, demonstrating SILC applied to a system without real-time feedback.

The three major subsystems – e-jet, AFM, and translational stages – work in a sequence that is coordinated by a central controller (Fig. 4). The following steps are performed in each iteration:

Step 1. **E-jet fabrication.** Fabricate a registration mark and desired structure.

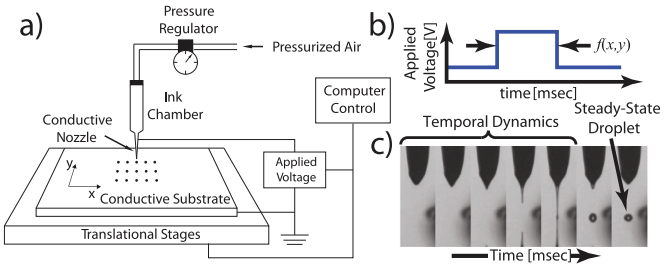

Fig. 3. Schematic of a typical e-jet system and ink droplet deposition process. a) Droplet ejection is controlled by an electrical field applied across the airgap between the nozzle and the substrate. b) A single droplet is deposited onto the substrate by raising the voltage from baseline voltage to activation voltage for a pulse width time of $f(x, y)$. c) Within a voltage pulse, the electrical field pulls the ink at the nozzle tip into a cone termed a *Taylor Cone*. The ink at the tip of the Taylor Cone is then ejected onto the substrate.

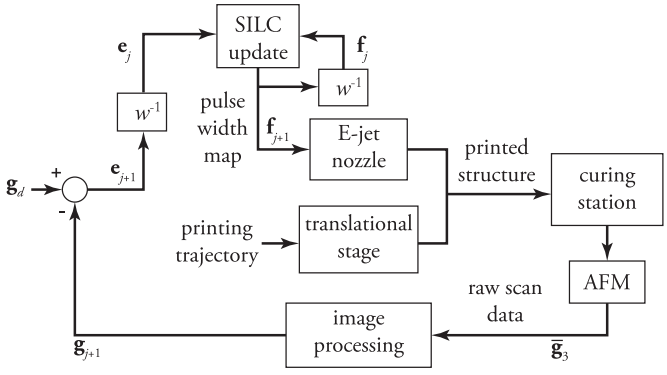

Fig. 4. High-level coordination scheme to close the SILC loop. w is the iteration shift operator.

(a) Shuttle the substrate such that a *blank* substrate location is under the e-jet print head; denote location as (x_0, y_0). E-jet print a 3 × 3 array of individual droplets, with pitch d, to serve as a registration mark (Fig. 5a).
(b) (optional) Shuttle substrate so that (x_0, y_0) is under the ultraviolet (UV) light curing station. Cure.
(c) Shuttle substrate so that (x_0, y_0) is under the AFM scanner. Scan the mark and store data as function $\bar{g}_1(\bar{x}, \bar{y})$; $\bar{x}$ and $\bar{y}$ are discretized coordinates in the x- and y-axes, but at a smaller discretization distance.
(d) Shuttle substrate so that location $(x_0, y_0 - a)$ is under the AFM scanner (Fig. 5a). Scan the fabrication area and store the data as $\bar{g}_2(\bar{x}, \bar{y})$ to establish the substrate topography.
(e) Shuttle substrate so that $(x_0, y_0 - a)$ is under the e-jet printer.
(f) Deposit structure. x- and y-axes are driven by an iteration-invariant trajectory. E-jet printhead actuation is driven by a 2-D input map, f_j, which is updated at each iteration.
(g) (optional) Shuttle substrate so that $(x_0, y_0 - a)$ is under the UV curing station. Cure.

Step 2. **Topography measurement.** Shuttle substrate so that $(x_0, y_0 - a)$ is under the AFM scanner. Scan the structure and store the data as $\bar{g}_3(\bar{x}, \bar{y})$.
Step 3. **Image processing.** Process the raw AFM data ($\bar{g}_1$, $\bar{g}_2$, and $\bar{g}_3$) using a sequence of image processing algorithms (Section 3.6) to generate the measured output map, g_j, from which the error map, e_j, is computed.
Step 4. **SILC update.** Apply SILC update law, Eq. (2), to compute a new input function, f_{j+1}.

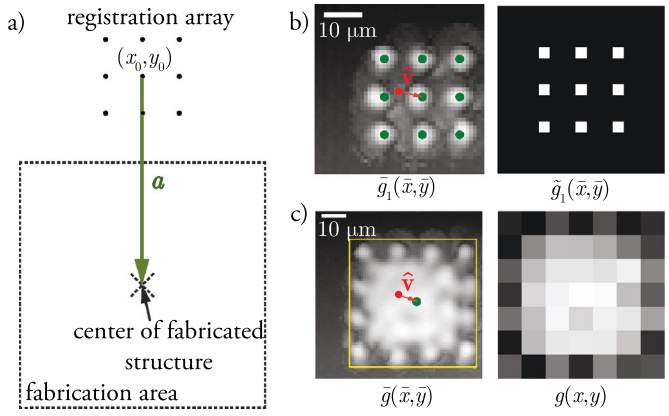

Fig. 5. Registration and image processing. a) A 3×3 registration dot array is deposited at location (x_0, y_0). Fabricated structures are printed at location $(x_0, y_0 - a)$. b) AFM scan image of the registration array, $\bar{g}_1$, and an ideal topography map, $\tilde{g}_1$, termed the kernel here. White pixels denote the highest measured height and black denote the lowest measured height. The green dots represent the overlayed kernel found using the algorithm in Eqs. (5) and (6). The offset vector, $\hat{v}$, denotes that the difference between the nominal registration array location, $\bar{v}$, and the actual array location. c) AFM image of a fabricated structure. Vector $\hat{v}$ denotes the offset between nominal and actual structure location. The yellow square denotes the truncated map. Right image is the register ed and image processed output g. (For interpretation of the references to colour in this figure legend, the reader is referred to the web version of this article.)

3.2. E-Jet subsystem

E-jet is a μ-AM tool that is capable of fabricating structures from functional materials with feature sizes down to the nanoscale [5]. In comparison, an ink-jet printer has a $\sim 30\,\mu$m resolution [14]. Importantly, e-jet feature sizes are on a comparable lengthscale to fabrication resolutions of lithographic micromachining, making e-jet a compelling technology for fabrication of biological micro-assays [21], charge printing for self assembly [22], electronics [23,24] and many others [25,26].

Fig. 3a shows a schematic of a typical e-jet system, which is composed of a conductive nozzle, a conductive substrate, translational stages, ink chamber, pressure supply to modulate ink chamber back pressure, and a voltage controller. The xy plane (substrate) is discretized into a normal grid and microscale structures are fabricated by depositing droplets at the discretized locations. Each single droplet is ejected onto the substrate by controlling the voltage between the conductive nozzle and substrate; in the mode used here, the nozzle is positioned at coordinate (x, y) and the voltage is pulsed from the baseline voltage V_{low} to the activation voltage V_{high} for the period of $f(x, y)$ milliseconds. During the pulse, the ink material at the nozzle tip is pulled into a conical shape, termed a *Taylor Cone*, and then ink is ejected from the tip of the cone, which then impinges on the substrate. In contrast to ink-jet printing which results in spherical droplets, defined by surface tension, e-jet yields a finer resolution because the ink ejects out of the tip of the *Taylor Cone*.

3.3. AFM Subsystem

As shown in Fig. 2, the AFM subsystem is mounted next to the e-jet system so that it can provide the feedback signal, g_j, at each iteration. Here we use a commercial tip-scanning AFM (Nanosurf NaniteAFM) with controller (Nanosurf C3000) and custom-written image processing algorithm (Section 3.6). The NaniteAFM is particularly attuned to integration with μ-AM fabrication as it has a large scan area (110 μm × 110 μm × 22 μm, $x \times y \times z$). It can achieve down to sub-one nanometer resolution [27], although the feature size of interest in e-jet is generally on the order of 100 nm and thus we can run the scans at a fast scan rate of ~ 50 μm s^{-1}. The AFM is driven by the Nanosurf C3000 controller

and application program interface (API) that allows us to automatically drive the AFM with a custom-written Python script.

3.4. Translation stages

The *x, y*, and *z* stages (*xy*: Aerotech PlanarDL-200XY; *z*: Aerotech ANT130-5-v) are in a serial, stacked kinematic arrangement where the *y*-axis carries the *z*-axis and the *x*-axis carries the *y*- and *z*-axes. This system has an accuracy of 0.1 μm and resolution of 0.01 μm, providing dynamic and static position control that is significantly better than the typical length scale used for e-jet fabrication, order of 100 nm, hence we assume perfect positioning control in our applications. The stages are driven by an Aerotech A3200 controller.

3.5. Integration

The entire system is coordinated via a central computer and custom-written Python script. Ancillary hardware is driven by spare digital and analog I/O from the Aerotech A3200. Ancillary hardware includes: a UV curing station (Dymax BlueWave 200 Ver. 1.1), a camera (Basler acA640-750um USB 3.0 camera, with Edmond Optics VZM1000i zoom imaging lens), an illumination source (AmScope LED-6W Gooseneck), and a pressure regulator (Wilkerson ER1-03-P000).

3.6. Registration and image processing

The print and scan sequence in Steps 1 and 2 of Section 3.1 provides three AFM scans: registration array scan $\bar{g}_1(\bar{x},\bar{y})$, blank substrate scan $\bar{g}_2(\bar{x},\bar{y})$, and printed structure scan $\bar{g}_3(\bar{x},\bar{y})$. Arguments $\bar{x}$ and $\bar{y}$ denote a coordinate in the *x* and *y* direction, respectively, but sampled at the AFM-scan discretization interval of 1 μm, which is of higher resolution than the discretization defined for the spatial dynamics. These three scans provide the information necessary to register the e-jet and AFM frames-of-reference – each pulled glass capillary nozzle has a different tip centroid relative to the mount and this difference must be accounted for – and compute the fabricated structure topography relative to the substrate.

3.6.1. Registration

Image registration leverages image processing routines and precise knowledge of stage positioning as it is shuttled between different locations in Steps 1 and 2. The nominal offset vector between the centroid of the nozzle tip and the AFM scan is assumed to be given by a fixed $\bar{\mathbf{v}} = \left[\bar{v}_x\mathbf{i}, \bar{v}_y\mathbf{j}, \bar{v}_z\mathbf{k}\right]$, where **i, j**, and **k** are unit vectors in the *x*-, *y*-, and *z*-axes directions, and $\bar{v}_x$, $\bar{v}_y$, and $\bar{v}_z$ are the corresponding entries of $\bar{\mathbf{v}}$ in the *x*-, *y*-, and *z*-axes directions, respectively. The actual offset vector $\mathbf{v} = \left[(\bar{v}_x - \hat{v}_x)\mathbf{i}, (\bar{v}_y - \hat{v}_y)\mathbf{j}, (\bar{v}_z - \hat{v}_z)\mathbf{k}\right]$ is computed by measuring the difference in location between an idealized registration array topography and the measured registration array topography. Given an array pitch, *d*, and the known relationship between AFM discretized coordinates and the actual distance, pixels per μm *ppm*, an idealized topography map, $\tilde{g}_1(\bar{x},\bar{y})$, is generated by creating a binary kernel with white pixels (value of 1) in a 3 × 3 array with a pitch of $d \times ppm$ and black pixels (value of 0) everywhere else (Fig. 5b). *x*- and *y*-axis offsets are found by searching for the offsets that maximize the convolution sum between $\bar{g}_1$ and kernel $\tilde{g}_1$,

$$\{\hat{v}_x, \hat{v}_y\} = \arg\max_{\bar{x},\bar{y}} \left\| \sum_{\substack{m\in\mathbb{Z}_M \\ n\in\mathbb{Z}_N}} \bar{g}_1(m,n)\tilde{g}_1(\bar{x}-m, \bar{y}-n) \right\|_F, \tag{5}$$

where $\|\cdot\|_F$ denotes the matrix Frobenius norm. *z*-axis registration is performed by simply subtracting the background scan, $\bar{g}_2$, from the structure scan, $\bar{g}_3$. Taken together, a registered structure topography map is given by

$$\bar{g}(\bar{x},\bar{y}) = \left(\bar{g}_3 - \bar{g}_2\right)\left(\bar{x} - \hat{v}_x, \bar{y} - \hat{v}_y\right). \tag{6}$$

Table 1
Reference Function Parameters.

Name	Size	Pitch [μm]
g_d^1, Postage Stamp	7 × 7	7
g_d^2, Notre Dame	11 × 11	5
g_d^3, Michigan	11 × 11	5
g_d^4, Ohio State	11 × 11	5

Table 2
Experimental update law designs and reference signals.

Ref.	q [nm^{-2}]	s [ms^{-2}]	r [ms^{-2}]	R_{RMC} [dB]
g_d^1	1	10^0	10^0	−33.60
g_d^1	1	10^1	10^0	−13.60
g_d^1	1	10^0	10^1	−34.54
g_d^1	1	10^0	10^2	−37.66
g_d^1	1	10^{-4}	10^{-2}	−113.60
g_d^2	1	10^1	10^1	−14.64
g_d^3	1	2×10^1	10^1	−8.64
g_d^4	1	2×10^1	10^1	−8.64

3.6.2. Image processing

As defined in Section 3.1, the measured output function *g* is the downsampled version of the measured topography. $\bar{g}$ provides us with a measured signal with both a higher sampling resolution and larger domain. We first truncate the map to the domain of *x* and *y* and then downsample $\bar{g}$ by numerical integration over a pixel domain,

$$g(x,y) = \frac{1}{R^2} \sum_{\bar{x}=R(x-\frac{1}{2})+1}^{R(x+\frac{1}{2})} \sum_{\bar{y}=R(y-\frac{1}{2})+1}^{R(y+\frac{1}{2})} \bar{g}(\bar{x},\bar{y}),$$

where *R* is the product of the fabrication resolution (in μm) and *ppm*.

4. Experiment setup

The set of experiments is designed to be a representative examination of SILC and the RMC criterion. We test eight different NO-SILC designs in experiment and complement the experiments with simulation and evaluation of the RMC criterion.

4.1. E-Jet Configuration

The substrate is a 100 mm diameter doped silicon wafer (Ultrasil Lot U-11408, resistivity 0.005Ω cm to 0.020 Ω cm) with a thin SiO_2 film deposited by plasma-enhanced chemical vapor deposition. The nozzles (World Precision Instruments TIP2TW1-L) have a 2 μm inner diameter and are sputter-coated with a Au/Pd film. The standoff height between the nozzle and the substrate is 40 μm for all tests. V_{low} is 225 V and V_{high} is 575 V. The build material is Loctite 3526, a medium-viscosity (17.5 Pa S) UV- and visible light-curable modified acrylic adhesive. To shield the ink from high energy visible light, amber syringe barrels (Nordson EFD Optimum 3cc) are used and opaque electrical tape is wrapped around exposed regions.

4.2. Reference functions

We use four different reference functions, g_d^1 – g_d^4; the set spans a range of frequency content and discretization intervals. Each function specifies a desired average topography height over each pixel: topographical maps are given in Fig. 6 and the domain sizes and function pitches are tabulated in Table 1. The Postage Stamp reference, g_d^1, is a simple, mostly flat topography to test the basic relationship between NO-SILC gain selection and iteration-domain performance. Institutional logos are used to demonstrate more complicated reference maps: g_d^2 (Notre Dame), g_d^3 (Michigan), and g_d^4 (Ohio State).

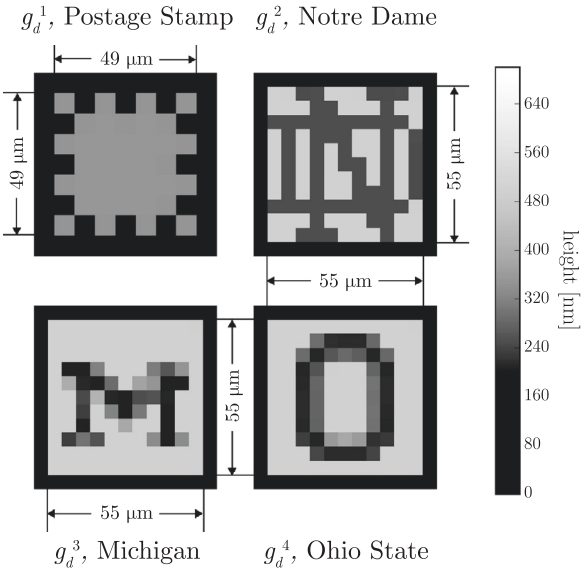

Fig. 6. Reference functions used in the experiments. The "Postage Stamp" map is used to evaluate different NO-SILC designs. The three institution maps are used to demonstrate SILC for a more complicated reference map. Grayscale intensity is a linear interpolation between 0 nm height (black) and 700 nm height (white).

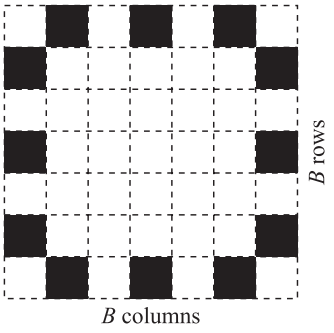

Fig. 7. System identification input generation matrix $\bar{f}$. White pixels denote a value of 1 and black pixels denote a value of 0.

4.3. System identification

NO-SILC is a model-based update law. Accordingly, we perform a set of experiments to identify a plant model h_o, $\underline{h}$, and $\bar{h}$ for integration into the update law in (3) and bound model uncertainty for RMC criteria evaluation. The different reference trajectories, g_d, have different discretization pitches (Table 1) that influence the spatial interactions between droplets. As such, system identification is run for both 5μm and 7 μm discretization pitches. The input function is given by Fig. 7, denoted by discretized $B \times B$ function $\bar{f}$, which is a binary matrix in which a 0 denotes no actuation voltage and a 1 denotes actuation voltage. A total of $n = 5$ independent experiments are performed for the 5 μm pitch and $n = 10$ for the 7 μm pitch functions, where each experiment has a different voltage pulse width, T_i,

$$
\begin{aligned}
f_i(x, y) &= T_i \bar{f}, \quad i = 0, 1, \ldots, n-1 \\
T &= \{25, 30, \ldots, 45\}\text{[ms]for5μm pitch} \\
T &= \{25, 30, \ldots, 45, 25, 30, \ldots, 45\}\text{[ms]} \\
&\quad \text{for 7 μm pitch.}
\end{aligned}
$$

The set of system identification patterns are printed and scanned using the basic procedure outlined in Section 3.1. Processed outputs maps are denoted g_i.

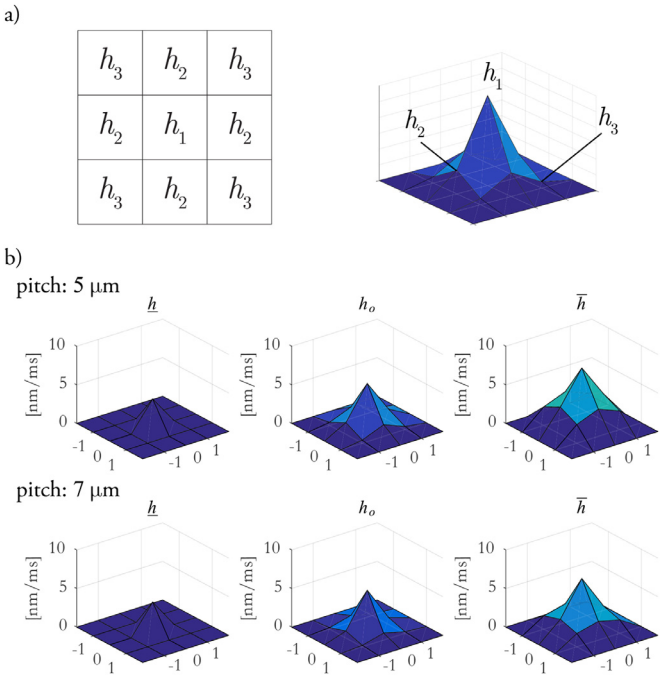

Fig. 8. Spatial impulse response models, h_o, $\underline{h}$, and $\bar{h}$. (a) Based on the symmetry and size assumptions, h_o is a 3×3 function with only three unique values, h_1, h_2, and h_3, hence three degrees of freedom. (b) Identified models, h_o, $\underline{h}$, and $\bar{h}$ for both pitches.

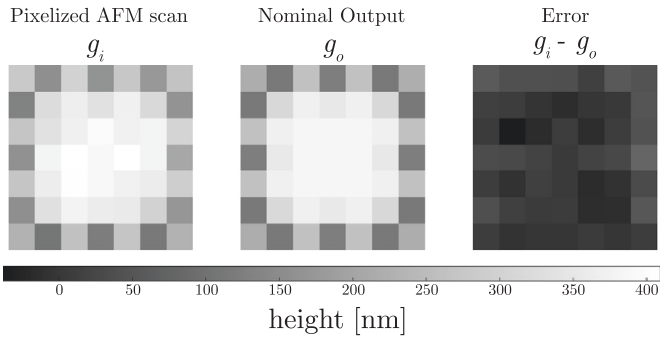

Fig. 9. Case comparison between measured output, g_i, and nominal output, g_o, for $T_i = 40$ ms and a pixel pitch of 7 μm.

4.3.1. Nominal model identification

We apply two assumptions when identifying a nominal model h_o: 1) h_o is symmetric about the center pixel and 2) a 3×3 dimension h_o captures the spatial dynamics. Both assumptions are supported by observations. Hence, the nine-pixel model is completely defined by three pixel height classes, (h_1, h_2, h_3), and thus has three degrees of freedom, (Fig. 8a).

Unknowns h_1, h_2, and h_3 are identified by minimizing the normed difference between the nominal outputs using the model with the structure in Fig. 8 and the experimental outputs, over the set of all n identification prints,

$$\min_{h_1,h_2,h_3} \|\|(g_0 - g_{o,0})/T_0\|_F, \|(g_1 - g_{o,1})/T_1\|_F, \ldots, \|(g_{n-1} - g_{o,n-1})/T_{n-1}\|_F\|_2$$

where

$$g_{o,i}(x, y) = (f_i * h_o)(x, y), \quad i = 0, 1, \ldots, n-1.$$

$\|\cdot\|_2$ denotes the vector 2-norm. Fig. 9 shows a case comparison between measured output g_i and the nominal output, $g_{o,\,i}$.

4.3.2. Model uncertainty identification

The nominal model system identification in the previous section, Section 4.3.1, can be leveraged to identify model uncertainty. The actual model, h, is expressed in the form of additive uncertainty,

$$h = h_o + \hat{h}, \tag{7}$$

where

$$\hat{h} \sim \mathcal{N}(0, \sigma^2)\mathbf{1}(3,3) \sim \mathcal{N}(0, \sigma^2)\begin{bmatrix} 1 & 1 & 1 \\ 1 & 1 & 1 \\ 1 & 1 & 1 \end{bmatrix}$$

and $\mathcal{N}(0, \sigma^2)$ is a random variable with a standard normal distribution, mean of 0 and variance of σ^2. An estimation of the plant variance σ^2 can be obtained using the system identification data,

$$\sigma^2 = \frac{1}{289n}\sum_{i=0}^{n-1} \|(g_i - g_{o,i})/T_i\|_F^2,$$

in which the division by $298n$ normalizes the sum by all measurements taken: there are n experiments performed and 289 convolution sum evaluations for the specific $\bar{f}$ map in Fig. 7. Given that our system identification method cannot directly identify the impulse response bounds, the vertex impulse response model is estimated to be $\{\underline{h}, \bar{h}\} = \{h_o - 3\sigma\mathbf{1}(3,3), h_o + 3\sigma\mathbf{1}(3,3)\}$; the vertex model thus bounds greater than 99% of the experimentally identified uncertainty in the model. This model is used in the RMC criterion verification and the study of RMC radius R_{RMC}.

4.4. Experimental methods

NO-SILC is evaluated in experiment using the system detailed in Section 3 and materials and configuration detailed in Section 4.1. We test a sampling of NO-SILC designs (Table 2) and reference signals $g_d^1 - g_d^4$.

4.5. Simulation methods and RMC criterion evaluation

Simulations of each NO-SILC design in Table 2 use (7) as the plant model and simulate 100 independent simulations of 20 iterations: the convolution kernel, h, is randomly selected using $\hat{h} \sim \mathcal{N}(0, \sigma^2)\mathbf{1}(3,3)$ at each coordinate (x, y) in every single convolution sum evaluation. The RMC criterion in Section 2.5.2 is evaluated for each NO-SILC design in Table 2; (7) is used for the plant in the criterion evaluation.

5. Experimental results

5.1. Experimental results

5.1.1. Reference g_d^1

The set of experiments investigating different NO-SILC update law designs applied to the Postage Stamp reference, g_d^1, agree with the conventional understanding of NO-SILC penalty terms r and s. Fig. 10 demonstrates the normalized Frobenius norm of the error function as a function of iteration. By increasing the penalty on input function ($s = 10^1$ compared to $s = 10^0$), the converged error norm rises from approximately 0.13 to approximately 0.20. Qualitatively, increasing the penalty on the convergence rate (increasing r), decreases the convergence rate. Although the difference between convergence rate is not appreciable for $r = 1$ and $r = 10$, a slower convergence rate can be observed when r is increased to 100. Note that the RMC criterion is not satisfied for all NO-SILC designs specified (all R_{RMC} values are negative, Table. 2). The RMC criterion is a sufficient, but not necessary condition for monotonic convergence of interval uncertain systems; clearly there are designs that will yield a nice, convergent signal in the iteration domain, despite there not being a guarantee of monotonic convergence. However, there is one design, the $(q, s, r) = \left(10^0, 10^{-4}, 10^{-2}\right)$

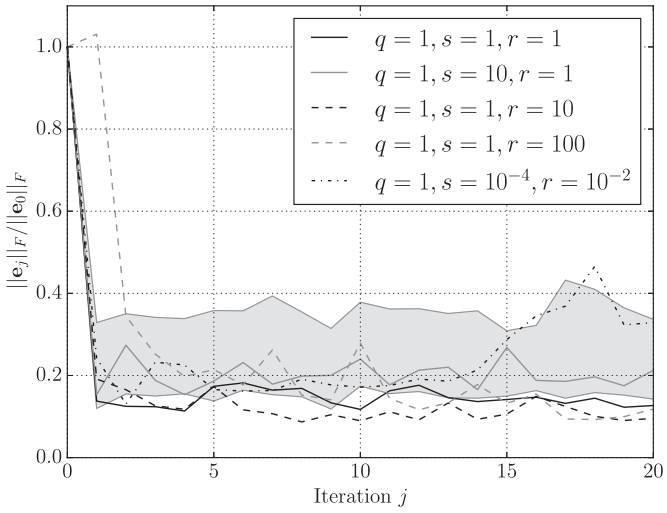

Fig. 10. Normalized Frobenius norm of the error function for 20 iterations for the Postage Stamp reference, g_d^1. The shaded area denotes the extents of the iteration-domain data for 100 independent SILC simulations with $q = 1, s = 10, r = 1$. Other simulation results are omitted for clarity.

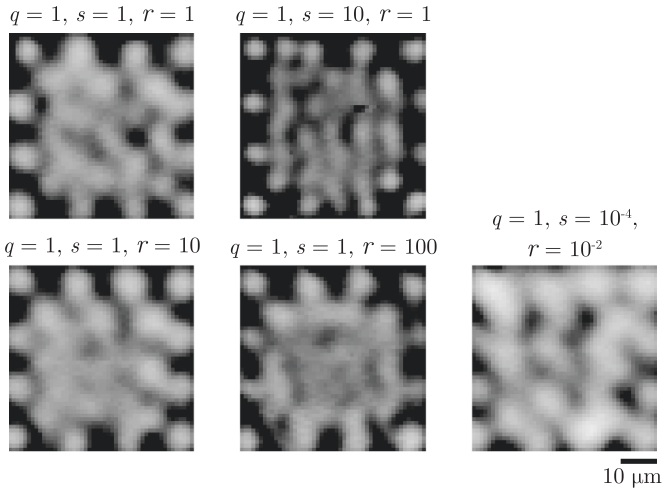

Fig. 11. Processed AFM images, $\bar{g}(\bar{x}, \bar{y})$, of the iteration 20 output of five NO-SILC designs. Grayscale intensity is a linear interpolation between 0 μm height (black) and 700 μm height (white). The dimension is 49 μm × 49 μm. The $(q, s, r) = \left(10^0, 10^{-4}, 10^{-2}\right)$ experiment demonstrates a non-convergent result.

design, that has an appreciably large in magnitude R_{RMC} value. Interestingly, this design corresponds to the only iteration-domain response that indicates a non-monotonic response; after an initial decrease in the Frobenius norm of the error function, there is then an increase in norm after approximately 13 iterations. The input function diverges as well (data not shown). A selected simulation result is plotted in Fig. 10 with $(q, s, r) = \left(10^0, 10^1, 10^0\right)$. Other simulation results are omitted for clarity. The interval uncertainty radius $||(\overline{\mathbf{H}} - \underline{\mathbf{H}})/2||_2$ is large for the e-jet application. We observed $||(\overline{\mathbf{H}} - \underline{\mathbf{H}})/2||_2$ to be 28.7% of the largest value of $\mathbf{H_o}$, compared to reported uncertainty intervals of approximately 11% in a temporal ILC application to a positioning system [19]. Consequently, both the simulation and experimental results have a have large random variation in the Frobenius norm of the error function, dithering around the converged value (Fig. 10).

Spatial domain results demonstrate the fabrication accuracy of the e-jet/AFM system with SILC compensation. Processed AFM scans of the final outputs (Iteration 20) are plotted in Fig. 11 and the corresponding processed output functions, g, and the reference image are plotted

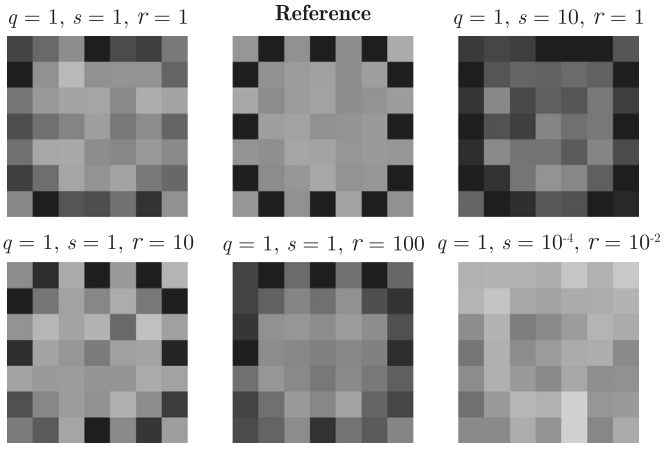

Fig. 12. Image processed output functions, $g(x, y)$, of the iteration 20 output of five NO-SILC designs and the reference function. Grayscale intensity is a linear interpolation between 0 nm height (black) and 700 nm height (white).

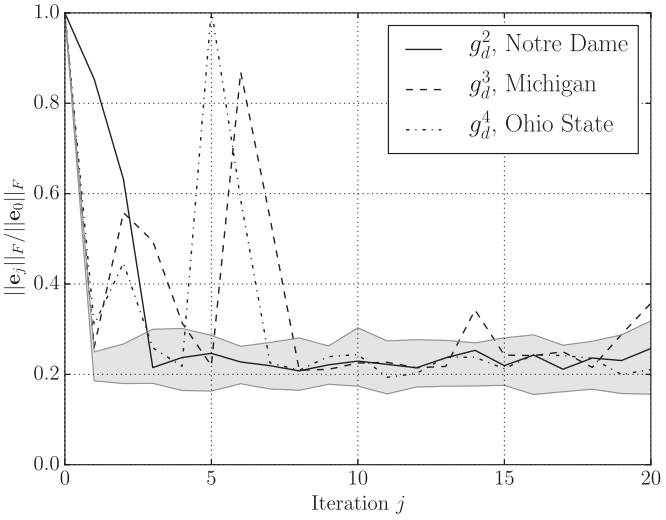

Fig. 13. Normalized Frobenius norm of the error function for 20 iterations for experiments with reference functions $g_d^2 - g_d^4$. The shaded area denotes the extents of the iteration-domain data for 100 independent SILC simulations for g_d^2 (Notre Dame). Other simulation results are omitted for clarity.

in Fig. 12. Absolute topographical accuracy ($\max(|e_{20}(x, y)|)$, for all convergent experiments and all x, y) for reference g_d^1 is 112.969 nm. The non-convergent experiment $(q, s, r) = (10^0, 10^{-4}, 10^{-2})$ clearly shows that too much material is ejected (Figs. 11 and 12).

5.1.2. Reference $g_d^2 - g_d^4$

The experiments conducted with the 5 μm resolution institutional logo reference functions demonstrate some interesting and beneficial robustness behavior of SILC. In general, the iteration- and spatial-domain behavior is qualitatively similar to the lower resolution Postage Stamp reference, g_d^1 (compare Figs. 10–12 to Figs. 13–14). However, on two occasions an unplanned and unpredictable error happened and then the e-jet/AFM/SILC system was able to recover from the error. On iteration 5 of the g_d^4 test, the AFM had a tip error, a common and deleterious measurement artifact in AFM [28], yielding an erroneous output function measurement (Fig. 15); the 6th iteration input overcompensated for this measurement error and ejected too much material, but the 7th iteration input recovered such that the error function matched the converged performance (Figs. 13 and 15). On Iteration 6 of the g_d^3 test, the ink ejection dynamics suddenly changed; again, the 7th iteration overcompensated and then the 8th input yielded an output that matches the final converged performance (Figs. 13 and 15).

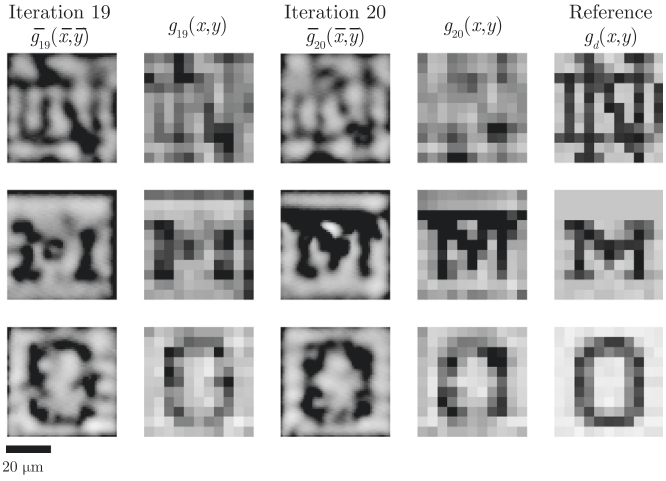

Fig. 14. Output functions from iterations 19 and 20. The die dimension is 55 μm × 55 μm for all three reference functions. Grayscale intensity is a linear interpolation between 0 nm height (black) and 700 nm height (white).

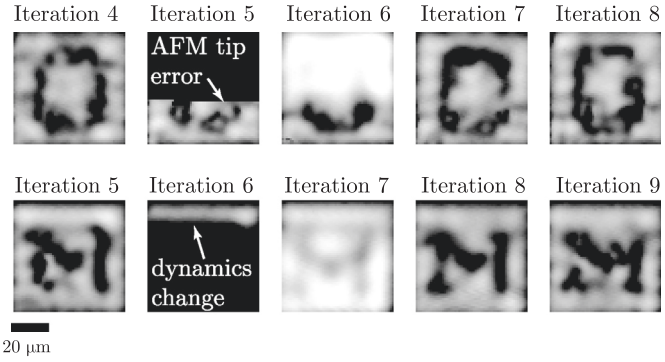

Fig. 15. SILC successfully recovers from both a sensor fault and a change in the system dynamics. The upper row shows a sensor fault that happened at Iteration 5 of the g_d^4 experiment; the proper output is recovered within 2 iterations. The lower row shows a sudden system dynamic variation in Iteration 6 of the g_d^3 experiment; again, the proper output is recovered within 2 iterations. Grayscale intensity is a linear interpolation between 0 nm height (black) and 700 nm height (white).

6. Discussions and conclusions

The SILC update law and accompanying hardware demonstrate the ability to fabricate a desired structure with less than 113 nm topography error and 5 μm x- and y-axis resolution without human intervention, despite environmental, material, and process variability. This autoregulating feature is particularly important to the nascent field of μ-AM systems, where research-grade tools such as this e-jet system are typically controlled via user observation and heuristic tuning of parameters. By automatically controlling spatial input functions, we demonstrate the ability to fabricate complex, topographically shaped structures at the micro-scale; these capabilities have never before been demonstrated by an autonomous μ-AM system. Furthermore, the uncertainty interval for the e-jet system is large (28.7% of the nominal model), highlighting the need for SILC analysis frameworks that consider system uncertainty.

This first exploratory experimental demonstration of autonomous μ-AM systems using SILC opens up many directions. The obvious new direction is to extend the 2-D spatial framework to both 3-D spatial and spatiotemporal frameworks; however, as addressed in [2], the

computational load scales exponentially with each dimension added, necessitating computationally efficient frequency-domain implementations. Multi-layer structures and multi-material (hence multi-plant) systems will be required to realize the full potential of μ-AM and will drive new theory in layer-to-layer SILC and switched system SILC, and the analysis of stability and convergence, thereof. Lastly, at the micro-scale, complex physics yield plant dynamics and sensor readouts that are often stochastic and difficult to explain. μ-AM processes are thus sensitive and control strategies must be robust. The results here showed two case examples of where the SILC algorithm and e-jet / AFM system was able to recover from practical challenges at the microscale: a metrology fault and an abrupt change in the plant dynamics. The build and then measure paradigm demonstrated here opens up new directions in observer-based fault detection schemes that can automatically detect sensor or actuator failure and then compensate for or cull out-of-specification manufacturing.

Acknowledgment

This work was supported in part by National Science Foundation under Awards CMMI-1434660, CMMI-1434693, and GRFP-1256260 and by start-up funds from the University of Notre Dame and the University of Michigan.

References

[1] Altin B, Wang Z, Hoelzle DJ, Barton K. Robust Monotonically Convergent Spatial Iterative Learning Control: Interval Systems Analysis via Discrete Fourier Transform, Accepted to IEEE Trans Control Syst Technol, DOI:10.1109/TCST.2018.2868039.

[2] Hoelzle DJ, Barton KL. On spatial iterative learning control via two dimensional convolution: stability analysis and computational efficiency. IEEE Trans Control Syst Technol 2016;24(4):1504–12.

[3] Onses MS, Sutanto E, Ferreira PM, Alleyne AG, Rogers JA. Mechanisms, capabilities, and applications of high-resolution electrohydrodynamic jet printing. Small 2015;11(34):4237–66.

[4] Yao T-F, Duenner A, Cullinan M. In-line metrology of nanoscale features in semiconductor manufacturing systems. Precis Eng 2017;47:147–57.

[5] Park J, Hardy M, Kang SJ, Barton K, Adair K, Mukhopadhyay D, et al. High-resolution electrohydrodynamic jet printing. Nat Mater 2007;6:782–9.

[6] Liddle JA, Gallatin GM. Lithography, metrology and nanomanufacturing. Nanoscale 2011;3:2679–88.

[7] Poellmann MJ, Barton KL, Mishra S, Johnson AJW. Patterned hydrogel substrates for cell culture with electrohydrodynamic jet printing. Macromol Biosci 2011;11(9):1164–8.

[8] Park J-U, Lee S, Unarunotai S, Sun Y, Dunham S, Song T, et al. Nanoscale, electrified liquid jets for high-resolution printing of charge. Nano Lett 2010;10(2):584–91.

[9] Pannier CP, Diagne M, Spiegel IA, Hoelzle DJ, Barton K. A dynamical model of drop spreading in electrohydrodynamic jet printing. J Manuf Sci Eng 2017;139(11):111008.

[10] Carter W, Popell GC, Samuel J, Mishra S. A fundamental study and modeling of the micro-droplet formation process in near-field electrohydrodynamic jet printing. J Micro Nano-Manuf 2014;2(2):021005.

[11] Sutanto E, Shigeta K, Kim Y-J, Graf P, Hoelzle D, Barton K, et al. A multimaterial electrohydrodynamic jet (e-jet) printing system. J Micromech Microeng 2012;22(5).

[12] Tse L, Barton K. A field shaping printhead for high-resolution electrohydrodynamic jet printing onto non-conductive and uneven surfaces. Appl Phys Lett 2014;104(14):143510.

[13] Lu L, Zheng J, Mishra S. A layer-to-layer model and feedback control of ink-jet 3-d printing. IEEE/ASME Trans Mechatron, 2015;20(3):1056–68.

[14] van der Bos A, van der Meulen M-J, Driessen T, van der Berg M, Reinten H, Wijshoff H, et al. Velocity profile inside piezoacoustic inkjet droplets in flight: comparison between experiment and numerical simulation. Phys Rev Appl 2014;1:014004.

[15] Wang Z, Pannier C, Ojeda L, Barton K, Hoelzle DJ. An application of spatial iterative learning control to micro-additive manufacturing. In: 2016 American Control Conference (ACC). IEEE; 2016. p. 354–9.

[16] Gray RM. Toeplitz and circulant matrices: a review. Found Trends Commun Inf Theory 2006;2(3):155–239.

[17] Trapp GE. Inverses of circulant matrices and block circulant matrices. Kyungpook Math J 1973;13(1):11–19.

[18] Ahn HS, Moore KL, Chen Y. Iterative learning control: robustness and monotonic convergence for interval systems. Springer Science & Business Media; 2007.

[19] Ahn H-S, Moore KL, Chen Y. Stability analysis of discrete-time iterative learning control systems with interval uncertainty. Automatica 2007;43:892–902.

[20] Amann N, Owens D, Rogers E. Iterative learning control for discrete-time systems with exponential rate of convergence. IEE Proc 1996;143:217–24.

[21] Park J-U, Lee JH, Paik U, Lu Y, Rogers JA. Nanoscale patterns of oligonucleotides formed by electrohydrodynamic jet printing with applications in biosensing and nanomaterials assembly. Nano Lett 2008;8(12):4210–16.

[22] Onses MS, Song C, Williamson L, Sutanto E, Ferreira PM, Alleyne AG, et al. Hierarchical patterns of three-dimensional block-copolymer films formed by electrohydrodynamic jet printing and self-assembly. Nat Nanotechnol 2013;8(9):667–75.

[23] Lee S, Kim J, Choi J, Park H, Ha J, Kim Y, et al. Patterned oxide semiconductor by electrohydrodynamic jet printing for transparent thin film transistors. Appl Phys Lett 2012;100(10):102108.

[24] Jeong S, Lee J-Y, Lee SS, Seo Y-H, Kim S-Y, Park J-U, et al. Metal salt-derived in–ga–zn–o semiconductors incorporating formamide as a novel co-solvent for producing solution-processed, electrohydrodynamic-jet printed, high performance oxide transistors. J Mater Chem C 2013;1(27):4236–43.

[25] Lee D, Lee J, Shin PS, Yu YSY, Kim Y, Hwang J. Structuring of conductive silver line by electrohydrodynamic jet printing and its electrical characterization. J Phys Conf Ser 2008;142:012039.

[26] Jayasinghe S, Qureshi A, Eagles P. Electrohydrodynamic jet processing: an advanced electric-field-driven jetting phenomenon for processing living cells. Small 2006;2(2):216–19.

[27] NaniteAFM brochure. https://www.nanosurf.com/downloads/naniteafm-brochure.pdf; Accessed: September 26, 2016.

[28] Eaton P, West P. Atomic force microscopy. Oxford University Press; 2010.